

An adjoint-based optimization method for reducing the axial force of a reactor coolant pump^{*}

Jia-ming WANG¹, Peng-fei WANG^{†‡2}, Xu ZHANG¹, Xiao-dong RUAN¹, Xin FU¹

¹State Key Laboratory of Fluid Power & Mechatronic Systems, Zhejiang University, Hangzhou 310027, China

²School of Engineering, Zhejiang University City College, Hangzhou 310015, China

[†]E-mail: wangpf@zucc.edu.cn

Received Apr. 18, 2019; Revision accepted Oct. 21, 2019; Crosschecked Oct. 28, 2019

Abstract: To alleviate the wear of a thrust bearing in a reactor coolant pump (RCP) while ensuring the hydraulic performance of the pump, an adjoint-based optimization method is proposed in this study. This method reduces the axial force of the RCP impeller and synchronously improves the impeller's hydraulic efficiency. By combining the adjoint solution with the radial basis function (RBF)-based mesh deformation, the optimization proceeds along the gradient direction, which greatly reduces the time and cost of the calculation. In the adjoint method, the adjoint equations in the rotating coordinate system are established, a joint objective function of the head constraint, hydraulic efficiency, and axial force is expressed, and then the blade surface sensitivity to the joint objective function is determined. In the RBF mesh deformation, the control points on the blade strand are evenly spaced, which ensures the smoothness of the deformed 3D twisted blade. Using the proposed optimization method, the hydraulic axial force of the impeller is reduced by approximately 3.8%, while the hydraulic efficiency of a scaled RCP impeller is increased by approximately 3.2%, and the head remains at an almost constant value. The obtained results validate the feasibility of the adjoint method for optimizing the design of centrifugal pumps.

Key words: Reactor coolant pump (RCP); Adjoint method; Radial basis function (RBF); Axial force; Shape optimization
<https://doi.org/10.1631/jzus.A1900156>

CLC number: TH313


1 Introduction

The reactor coolant pump (RCP) is the “heart” of a nuclear reactor, and is the only high-speed revolving piece of equipment in the primary loop of a pressurized water reactor (Gao et al., 2013). Single-stage centrifugal RCPs with shaft seals, which are applied

in second-generation and second-plus-generation nuclear power plants, may have a trace radioactive spillover problem. The canned RCP (Rahim et al., 2012) adopted in the new-generation nuclear power technology developed by Westinghouse, USA, can completely eliminate nuclear leaks from the RCP. However, as bearings used in RCPs have a narrow internal space and low lubricant viscosity (Si et al., 2012), bearing wear and even failure easily occur; hence, the bearing capacity of the thrust bearings must be strictly limited. During the preliminary test of a third-generation RCP, the surface of the graphite thrust pad and hardened layer of the thrust disk were seriously worn, and even the graphite thrust pad was partially exfoliated. Previously conducted analysis revealed that this may be due to the overload axial force of the spindle (Li et al., 2016). In addition, the

^{*} Corresponding author

^{*} Project supported by the National Basic Research Program (973 Program) of China (No. 2015CB057301), the Zhejiang Provincial Natural Science Foundation of China (No. LQ18E060002), and the Science Fund for Creative Research Groups of the National Natural Science Foundation of China (No. 51821093)

 ORCID: Jia-ming WANG, <https://orcid.org/0000-0001-9931-0209>; Peng-fei WANG, <https://orcid.org/0000-0003-0957-3414>

© Zhejiang University and Springer-Verlag GmbH Germany, part of Springer Nature 2019

spindle axial force is the main cause of axial series motion, part wear, and vibration of the unit (Du et al., 2016). The hydraulic axial force acting on the impeller is the main component of the spindle axial force. Therefore, reducing the hydraulic axial force by optimizing the impeller design can improve the life of the bearing and the safety of the RCP.

In general engineering applications of fluid machinery, engineers often balance the axial force by using techniques including balancing the holes on impellers, back blades on impellers, balancing discs, and auxiliary impellers. For example, Li et al. (2012) designed an auxiliary impeller for a shielded pump. The auxiliary impeller drives circulation of the fluid in the cooling circuit and produces an axial force equal and opposite to the resultant force of the main impeller axial force and the rotor's weight, so that the axial force is eliminated. Kong et al. (2009) comprehensively analyzed and calculated the axial force of the rotor of a PBN65-40-250 shield pump. They found that the axial force can be balanced by adjusting the size of the seal ring behind the impeller and the flow area of the balance hole. Dong and Chu (2015) found that variations in the balance hole diameter have an impact on the head, efficiency, shaft power, and balance chamber pressure of a centrifugal pump. However, these traditional methods either increase the complexity of the structure (in the case of using a back blade or balance plate) or reduce the strength of the existing structures (in the case of using a balance hole), making them infeasible for an RCP owing to safety concerns. As the rotational speed and operating pressure of the RCP remain almost unchanged during normal operation, the hydraulic axial force generated by the impeller mainly depends on its geometric shape. Therefore, adjusting the design parameters of the impeller can aid in meeting the axial load requirements. For example, Zhou (2017) adjusted the impeller's outlet edge to obtain a high efficiency and low axial force. As changing the geometrical shape of the impeller directly affects the head and efficiency of the entire pump, it is necessary to take the head, efficiency, and axial force into consideration when designing the impeller, which is beyond the traditional hydraulic design methods of pumps.

With the development of computing technology, an increasing number of researchers have started to

use computational fluid dynamics (CFD)-based stochastic algorithms to optimize the design parameters of fluid machinery in recent years. For example, Derakhshan et al. (2013) used a global optimization method based on artificial neural networks and the artificial bee colony algorithm to redesign the geometry of the Berkeh 32-160 impeller, thus improving its hydraulic performance. Zhang et al. (2011) proposed a multi-objective optimization method that combined an artificial neural network and a non-dominated sorting genetic algorithm (NSGA-II) to improve the performance of a helical axial-flow multiphase pump. These methods, however, are time-consuming. As there is a complex relationship between the geometric parameters and the performance of the pump impeller, a large number of sample points need to be distributed in the design space, and each sample point requires re-geometric modeling, meshing, and a flow field calculation; furthermore, a large number of iteration steps are required to obtain the optimal result. In addition, owing to the limited number of design parameters selected by these stochastic algorithms, some geometric features of 3D twisted blades are neglected.

If the gradient relationship between the blade geometry and optimization objective can be obtained based on the flow field equations, the steepest descent method can be directly used to quickly optimize the blade based on the gradient information. This was first proposed by Jameson (1988), who solved the airfoil optimization problem with the adjoint method. In recent years, a large number of researchers have expanded the applications of the adjoint method. For example, Othmer (2014) developed a topology optimization for ducted flows and shape optimization for ducted as well as external flows in car aerodynamics. Papoutsis-Kiachagias and Giannakoglou (2016) developed the continuous adjoint method and applied it to turbulent incompressible flows for shape and topology optimization problems. When the adjoint method is applied to the optimization of a rotating impeller, it is necessary to establish corresponding adjoint equations that relate to the blade geometry and optimization objective in the rotating coordinate system while considering the centrifugal and Coriolis forces (Papoutsis-Kiachagias et al., 2014). Furthermore, mesh deformation technology should be used to update the geometry and mesh in each iteration of the

adjoint optimization. As the RCP blades are 3D twisted, the direct mesh stretching method can always result in concave and convex points on the boundary of the blades, which would cause deformation failure. Therefore, a new mesh updating method should be adopted for RCP optimization with adjoint methods (Poirier and Nadarajah, 2012).

In summary, an adjoint optimization method based on the radial basis function (RBF) mesh deformation is proposed to realize optimization of both the impeller axial force and efficiency without changing the hydraulic head of the RCP. Since this method can obtain the gradient information between the boundary geometry and the objective performance (Lotz et al., 2015), the highly sensitive areas can be figured out. In contrast to the traditional stochastic algorithms, which select several design parameters as optimization parameters, this method updates the geometry continuously and directly using the calculated gradient information. Its advantages are mainly embodied in the following two aspects: (1) It does not require a large amount of basic calculation data; therefore, it can reduce the workload and improve the efficiency. (2) In the optimization process, the gradient information of the geometric boundaries can aid in determining the influence of different regions on the objective function.

This paper is structured as follows. First, the adjoint method and the basic theory of the RBF mesh deformation are introduced. Then, the key steps of the RCP impeller optimization are introduced. At last, an analysis of the results of the optimization is presented, and the significance of this method is summarized.

2 Methodology

2.1 Surface sensitivities

For an impeller flow field, if a boundary is displaced, the distribution of velocity and pressure will change accordingly. Therefore, we can use the function $J(\mathbf{v}, p, \boldsymbol{\beta})$ (Liu et al., 2015) to represent the hydraulic performance of an impeller, where \mathbf{v} , p , and $\boldsymbol{\beta}$ represent relative velocity, static pressure, and the localized surface normal displacements, respectively. Similarly, the incompressible Navier–Stokes equations for steady-state flow in rotating coordinates can be expressed as $R(\mathbf{v}, p, \boldsymbol{\beta})=0$, as shown in Eq. (1). As $\boldsymbol{\beta}$

affects the geometry of the flow domain, it is not explicitly indicated in the equations.

$$\begin{cases} \nabla p + (\mathbf{v} \cdot \nabla) \mathbf{v} - \nabla \cdot [2\gamma D(\mathbf{v})] + 2\boldsymbol{\omega} \times \mathbf{v} + \boldsymbol{\omega}^2 \mathbf{r} = 0, \\ \nabla \cdot \mathbf{v} = 0, \end{cases} \quad (1)$$

where γ is the kinematic viscosity, $D(\mathbf{v}) = [\nabla \mathbf{v} + (\nabla \mathbf{v})^T]/2$ is the rate of the strain tensor, $\boldsymbol{\omega}$ is the vector of the angular velocity, and \mathbf{r} represents the radius vector of the grid.

If the derivative of $J(\mathbf{v}, p, \boldsymbol{\beta})$ to $\boldsymbol{\beta}$ is calculated, we will obtain the gradient between the normal displacements of the impeller surface and its hydraulic performance, and then use it for optimization. However, because of the implicit relationship between \mathbf{v} , p , and $\boldsymbol{\beta}$, it is difficult to obtain the derivative directly. Therefore, we introduce a Lagrange multiplier $\lambda = (\mathbf{u}, q)$ to a Lagrange function L including J and R as

$$L = J + \int_{\Omega} (\mathbf{u}, q) R d\Omega = J, \quad (2)$$

where \mathbf{u} and q are called the adjoint velocity and the adjoint pressure, respectively, and Ω represents the flow domain.

To obtain the derivative of the objective function with respect to $\boldsymbol{\beta}$, it is necessary to eliminate the last two terms on the right side of Eq. (3), which is the partial differential equation of L . Therefore, if the sum of these two terms is zero, we can obtain the constraint equation Eq. (4).

$$\delta L = \delta_{\boldsymbol{\beta}} L + \delta_{\mathbf{v}} L + \delta_p L, \quad (3)$$

$$\delta_{\mathbf{v}} J + \delta_p J + \int_{\Omega} (\mathbf{u}, q) \delta_{\mathbf{v}} R d\Omega + \int_{\Omega} (\mathbf{u}, q) \delta_p R d\Omega = 0. \quad (4)$$

The objective function J in Eq. (4) is replaced by an integral representation (Eq. (5)) with a boundary $\Gamma = \partial\Omega$ and an interior of Ω . Then, we can derive the adjoint equations (Eq. (6)) (with \mathbf{u} and q as the variables) from the integrals over the domain and the adjoint boundary conditions (Eq. (7) at the inlet and wall, and Eq. (8) at outlet) from the vanishing of the boundary integrals.

$$J = \int_{\Gamma} J_{\Gamma} d\Gamma + \int_{\Omega} J_{\Omega} d\Omega, \quad (5)$$

$$\begin{cases} \nabla q - 2D(\mathbf{u})\mathbf{v} - \nabla \cdot [2\gamma D(\mathbf{u})] - 2\boldsymbol{\omega} \times \mathbf{u} = -\frac{\partial J_\Omega}{\partial \mathbf{v}}, \\ \nabla \cdot \mathbf{u} = \frac{\partial J_\Omega}{\partial p}, \end{cases} \quad (6)$$

where $2D(\mathbf{u})\mathbf{v} = \nabla \mathbf{u} \cdot \mathbf{v} + (\mathbf{v} \cdot \nabla) \mathbf{u}$ and $2D(\mathbf{u}) = \nabla \mathbf{u} + (\nabla \mathbf{u})^T$.

$$\begin{cases} \mathbf{u}_t = 0, \\ u_n = -\frac{\partial J_\Gamma}{\partial p}, \\ \mathbf{n} \cdot \nabla q = 0, \end{cases} \quad (7)$$

$$\begin{cases} q = \mathbf{u} \cdot \mathbf{v} + u_n v_n + \gamma(\mathbf{n} \cdot \nabla) u_n + \frac{\partial J_\Gamma}{\partial v_n}, \\ 0 = v_n \mathbf{u}_t + \gamma(\mathbf{n} \cdot \nabla) \mathbf{u}_t + \frac{\partial J_\Gamma}{\partial \mathbf{v}_t}, \end{cases} \quad (8)$$

where subscripts t and n indicate the tangential and normal directions, respectively, and \mathbf{n} is the unit normal vector of the mesh surface.

The adjoint equations (Eq. (6)) are similar to the Navier–Stokes equations in the rotating coordinate system. Therefore, given the expression of J , the items on the right side are both known, and they can thus be solved directly on the original grid data with a solver similar to that for the flow field calculation. It is worth noting that, in our study, the incompressible k - ε turbulent model is adopted. Turbulence parameters from flow calculations remain unchanged in adjoint calculations. Therefore, the variation in the eddy viscosity γ is neglected with a common approximation in the adjoint solution, which is known as “frozen turbulence” (Dwight and Brezillon, 2006).

According to the adjoint calculation results and Eq. (9),

$$\delta R = \delta_\beta R + \delta_v R + \delta_p R = 0, \quad (9)$$

we can compute the gradient of J with respect to the localized surface normal displacement β :

$$\delta_\beta L = \delta_\beta J - \int_\Omega (\mathbf{u}, q) \delta_v R d\Omega - \int_\Omega (\mathbf{u}, q) \delta_p R d\Omega. \quad (10)$$

As the last two items of Eq. (10) are the same as those in the Eq. (4), they satisfy the adjoint equations (Eq. (6)). If an objective function is independent of

the domain interior, the volume integral items in the detailed expansion of Eq. (10) will vanish. Besides, there is no explicit dependence of the objective function on the deformation ($\delta_\beta J = 0$), and \mathbf{u} equals zero at the wall. The derivative process of Eqs. (2)–(10) is similar to that of the equations of Othmer (2008), who expressed the surface sensitivities as

$$\delta_\beta L \propto \mathbf{u}_t^j \cdot \mathbf{v}_t^j, \quad (11)$$

where \mathbf{u}_t^j and \mathbf{v}_t^j are the tangential adjoint velocity and tangential velocity of grid j , which is the closest to the surface perturbation.

2.2 RBF-based mesh deformation

By coupling surface sensitivities with the geometric deformation method, it is possible to improve the performance of the fluid model. In this work, RBF-based mesh morphing is adopted to change the model geometry through mesh deformation. While taking the displacements of the control points as variables, the RBF calculates the displacements of the vertexes of the internal meshes, so that all the meshes can be smoothly deformed synchronously (Rao and Yang, 2017). In the shape optimization process, to obtain the displacements of the control points, it is necessary to transform the surface sensitivities into the gradients between the objective functions and position vectors of control points. The following section details the theory of RBF-based mesh deformation and the derivation of the gradients at control points.

The outline of the RBF-based mesh deformation is as follows. First, n control points on the blades are selected for controlling the deformation of the blades. The position vectors of these control points at each iteration step can be written as \mathbf{x}_i ($i=1, 2, \dots, n$), and their displacements to the next iteration can be written as \mathbf{s}_i ($i=1, 2, \dots, n$). The displacement of any internal mesh node with position \mathbf{x}' can then be formulated as

$$\mathbf{s}(\mathbf{x}') = \sum_{i=1}^n r_i \varphi(\|\mathbf{x}' - \mathbf{x}_i\|), \quad (12)$$

where $\|\mathbf{x}' - \mathbf{x}_i\|$ is the distance between the node \mathbf{x}' and the control point \mathbf{x}_i , r_i is the coefficient of the RBF, φ is the RBF, and Wendland's C2 function (Rendall and Allen, 2009) is adopted for its high

computational efficiency and good mesh deformation quality, which is expressed as

$$\varphi(\|\mathbf{x}' - \mathbf{x}_i\|) = (1 - \|\mathbf{x}' - \mathbf{x}_i\|)^4 (4\|\mathbf{x}' - \mathbf{x}_i\| + 1). \quad (13)$$

The gradients between the objective functions and position vectors of control points can be calculated by Eq. (14). The term $\delta_{\mathbf{x}}\boldsymbol{\beta}$ refers to the localized surface normal displacements of the model caused by changes in position vectors of control points, which can be obtained from the displacement equations (Eq. (10)) of RBF-based mesh deformation (Robinson et al., 2012).

$$\delta_{\mathbf{x}}L = \delta_{\boldsymbol{\beta}}L \cdot \delta_{\mathbf{x}}\boldsymbol{\beta}. \quad (14)$$

2.3 Shape optimization process

Once the gradient data is available, it is possible to calculate the displacements of the control points easily by using the steepest descent method. The basic iterative equation is

$$\mathbf{x}_i^* = \mathbf{x}_i + a\delta_{\mathbf{x}}L, \quad (15)$$

where a is the step size, and \mathbf{x}_i^* is the position vector of the i th control point after iteration.

During the entire optimization process, the function value changes monotonously with an increase in iteration times. The detailed operation steps for the impeller optimization are as follows (Hsin et al., 2010):

1. First, the initial calculation model is created according to the preliminary design scheme.
2. After setting the boundary conditions, the fluid calculation program is operated to converge iteratively.
3. With the velocity \mathbf{v} and pressure p data calculated in step 2, and given the boundary conditions of the adjoint operator, the adjoint equation is solved iteratively.
4. The calculation results of the adjoint operator are substituted into the gradient equations to obtain the gradients relationship between the objective function and position vectors of control points.
5. The calculation model is modified using RBF-based mesh deformation technology based on

the gradient data in step 4.

6. Steps 2–5 are repeated until the objective performance indicators meet the design requirements or the iterative curve has converged; the optimization results and model geometric data are then outputted.

It should be noted that the main program of this study is based on OpenFOAM (Open Field Operation and Manipulation) 2.2 (ESI-OpenCFD, 2007). OpenFOAM provides an object-oriented implementation of difference operators that can be invoked on any type of computing grid; as a result, a continuous adjoint can be operated in a straightforward manner (Othmer et al., 2007).

3 Optimization of the RCP impeller

In this study, we combined the adjoint method with the RBF-based mesh deformation to optimize the design of the RCP impeller. This approach reduces the hydraulic axial force and improves the efficiency of the impeller while keeping the hydraulic head at a constant value.

3.1 Preliminary design of RCP impeller

The parameters of the RCP are partially listed in Table 1, and the 1:2.5 scaled preliminary model was designed according to the design manual (Gülich, 2014). The initial blade model's parameters are listed in Table 2, and its shape is shown in Fig. 1.

We performed a validation of the external characteristics of the model pump. By comparing the simulated and tested flow-head curves (Fig. 2), it can be observed that the simulation results are consistent with those of the experiments (Su et al., 2017). Through the simulation, under rated working conditions, the initial design of the head meets the requirements of the scale, but the hydraulic efficiency is approximately 82.1%, which is lower than the efficiency design requirement of 85%, and the axial force is approximately 5700 N, which is very close to the limit of the scale axial force of 5730 N. Therefore, it is necessary to reduce the axial force and improve the hydraulic efficiency while maintaining the head at a roughly constant value.

To facilitate the optimization, a single channel from the impeller was extracted. According to the operation steps of the adjoint optimization in Section

2.3, a steady-state calculation is required in each iteration step. The detailed settings are as follows: The incompressible standard k - ε turbulence model is used

Table 1 Original and 1:2.5 scaled RCP parameters

Parameter	Description	
	Original	Scaled
Design pressure (MPa)	17.1	Atmospheric pressure
Design temperature (°C)	343	Atmospheric temperature
Rated flow (m ³ /h)	17 886	1144.7
Rated power (MW)	5.15	0.005 54
Rated head (m)	111.3	17.8 (impeller 21.75)
Rated speed (r/min)	1750	1750
Motor frequency (Hz)	60	60

Table 2 Preliminary design of the 1:2.5 scaled impeller

Parameter	Value
Inlet diameter (mm)	238.8
Shroud outlet diameter (mm)	313.6
Hub outlet diameter (mm)	223.2
Outlet edge width (mm)	76.4
Inlet angle (°)	46
Outlet angle (°)	34
Wrap angle (°)	120.8
Blade thickness (mm)	5



Fig. 1 Preliminary designed impeller

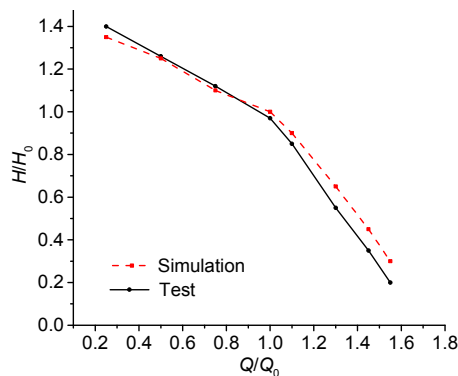


Fig. 2 Hydraulic performance comparison between test and simulation (H is the head, H_0 is the rated head, Q is the flowrate, and Q_0 is the rated flowrate)

in the flow simulation. A second-order scheme of the spatial discretization is adopted by software FLUENT. The convergence criterion is that residuals are less than 1×10^{-5} . Mass flow inlet is set at the inlet of the model. Pressure outlet is set at the outlet of the model. No slip walls are set at blade walls.

3.2 Expression of optimization objective

Before the adjoint calculation, according to Eq. (4), it is necessary to define the analytic expression of the optimization objective. In this study, three physical quantities were involved: the head, hydraulic efficiency, and axial force. Eq. (16) is the analytic expression of the head H , which is proportional to the mass-averaged total pressure difference ΔP between the inlet and outlet. Eq. (17) is the analytic expression of hydraulic efficiency η , which is the ratio of the output power to the input power. The input power is the product of the rotational speed and shaft torque, and the output power is the product of the volume flowrate and total pressure difference between the outlet and inlet. Eq. (18) is the analytic expression of the hydraulic axial force F_a , which is the area integral of the normal stress p and shear stress τ on both sides of the blade in the axial direction.

$$H = \frac{\Delta P}{\rho g} = \frac{\int_{\text{inlet, outlet}} \left(p + \frac{1}{2} \rho v^2 \right) \mathbf{v} \cdot \mathbf{n} d\Gamma}{\rho g}, \quad (16)$$

$$\eta = \frac{Q \rho g H}{n \cdot (2\pi/60) \cdot T}, \quad (17)$$

$$F_a = \int_{\text{blade}} (\mathbf{p} + \boldsymbol{\tau}) \cdot \mathbf{a} d\Gamma, \quad (18)$$

where ρ is the density of the fluid, g is gravitational acceleration, \mathbf{v} is the velocity vector, v is the value of the velocity, n is the rated speed, T is the value of the spindle torque, and \mathbf{a} is the unit axial vector.

To normalize each optimization objective, we regarded the performance parameters of the initial design model as the reference parameters and defined the analytic objective expressions for the head, hydraulic efficiency, and axial force in Eqs. (19)–(21), in which H_T represents the target head (the target head of the scale impeller model is 21.75 m according to hydraulic requirements). To combine these three objective functions into one, we use the simplest weight-averaged method, as shown in Eq. (22); the values of the weight factors k_1 , k_2 , and k_3 are discussed

in Section 3.4. The objective function is a surface integral over the boundary of the model, so the differential items of J_Q in Eq. (6) are zero. The adjoint boundary conditions for the inlet and wall are Eq. (23), and the outlet conditions are Eq. (24). Eq. (4) shows that the adjoint equations are transport equations that are similar to those governing the flow, so the same solver is applied. When the residuals of the adjoint operators are less than 1×10^{-5} , the calculation is stopped.

$$J_H = \frac{(H - H_T)^2}{0.01H_T^2}, \quad (19)$$

$$J_\eta = -\frac{\eta - \eta_0}{\eta_0}, \quad (20)$$

$$J_{F_a} = \frac{F_a - F_{a0}}{F_{a0}}, \quad (21)$$

$$J_m = k_1 J_H + k_2 J_\eta + k_3 J_{F_a}, \quad (22)$$

$$\begin{cases} u_t = 0, \\ v_n \left[-k_1 \frac{200(H - H_T)}{\rho g H_T^2} + k_2 \frac{T_0}{H_0 T} \right], & \text{at inlet,} \\ u_n = \begin{cases} -k_2 \frac{HT_0}{H_0} [(r \times n) \cdot a]^{-2} - k_3 \frac{1}{F_{a0}} n \cdot a, \\ 0, \end{cases} & \text{at blade boundary,} \\ 0, & \text{at other walls,} \\ n \cdot \nabla q = 0, \end{cases} \quad (23)$$

$$\begin{cases} q = u \cdot v + u_n v_n + \gamma (n \cdot \nabla) u_n + k_1 \frac{200(H - H_T)}{\rho g H_T^2} \left(\frac{v^2}{2} + v_n^2 \right), \\ 0 = v_n \left[u_t + k_1 \frac{200(H - H_T)}{\rho g H_T^2} v_t \right] + \gamma (n \cdot \nabla) u_t, \end{cases} \quad (24)$$

where η_0 , F_{a0} , and T_0 are the efficiency, axial force, and spindle torque of the initial model, respectively. J_m is the multi-objective function.

3.3 Setting of RBF-based mesh deformation

Owing to the large distortion of the blades, it is very important to distribute the control points reasonably to reflect the overall geometric features. Therefore, uniformly distributed control points on the middle surface between the pressure surface and suction surface of the blade are helpful in achieving excellent optimization. Based on the axial projection of

the impeller, the entire flow passage is evenly divided into 10 span intervals, and 67 control points are evenly selected on each of these 11 spans, as shown in Fig. 3. These control points are shifted according to sensitivity information; then, the pressure surface and suction surface of the blade are deformed simultaneously. As the distances from the control points to the two surfaces are the same, the blade thickness does not change substantially after the deformation. Besides, to maintain geometry constraints, other fixed control points are distributed on the undeformed boundaries.

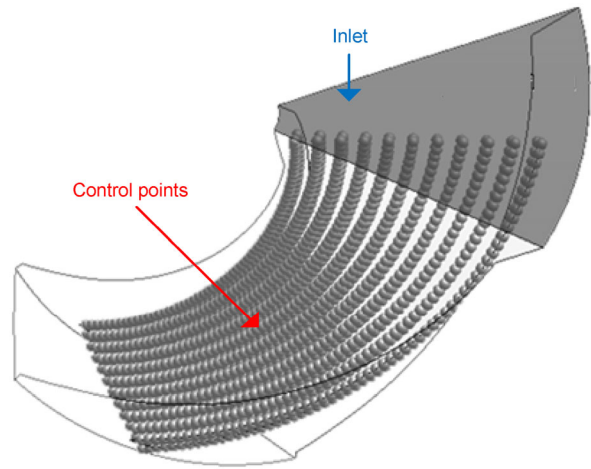


Fig. 3 Distribution of control points on the impeller surface

3.4 Factor of each objective function

According to the compositions of Eq. (22), the gradient vector of the multi-objective function is the weight sum of the gradient vectors of the head, efficiency, and axial force functions. Therefore, the gradient data corresponding to the multi-objective function is affected by the gradient distribution of each sub-function; some gradient vectors overlap and increase, while others cancel each other and then decrease. In the optimization iteration process, the trend of the structural deformation is affected by the weight of each objective function; thus, we can control the entire process by adjusting each weight factor. To determine the appropriate weight factor, it is necessary to perform a pre-experiment in the early stages of optimization. In the specific operation method, the weight factor of the head function is maintained as a constant, the orthogonal experiment method is used to distribute the sample points of the other two factors,

and the one-step adjoint optimization is performed for each sample point. The weight proportion was determined by comparing the changes in each objective function after model reconstruction; the orthogonal test records of the weight factors (Eq. (22)) are presented in Table 3, and a ratio of 1:70:70 was selected to ensure that the variation amplitudes of the efficiency and axial force were comparatively similar.

4 Analysis of results

4.1 Relations between various objective functions

There are relationships among the various objective functions. Therefore, to compare the influence of the different blade regions on each objective function, the adjoint solution of each objective function was solved. Through an analysis of the gradient data, we can accurately determine how the blade deformation affects these objective functions. As shown in Fig. 4, the dark color indicates that the areas deforming along the normal outward direction increase the objective function, and the opposite trend is indicated by a light color. The images of the axial force function and efficiency function overlap greatly. This is because the efficiency is related to the axial moment (Eq. (17)), which is the integral sum of the normal stress and shear stress centered at the axis, and the axial force is the integral sum of the normal stress and shear stress on the blade in the axial direction. Thus, the axial force function is positively correlated with the efficiency function. The images corresponding to the head function and axial force function have opposite colors near the outlet (the areas in the dashed circle in Fig. 4); this is because a change in the outlet angle may increase the head function, but reduce the axial force function. Therefore, it can be inferred that the multi-objective optimization can improve the axial force performance without changing the head.

4.2 Optimization results

In the entire iteration process, the flow field equations and adjoint equations were calculated repeatedly. On our computing platform (Intel i7-6700 CPU, 12G RAM), 500 steps (approximately 10 min) were required for each fluid calculation and 500 steps (approximately 30 min) were required for each adjoint calculation to achieve a given convergence condition. The steepest descent method (Tammisola and Juniper, 2015) and the gradient data were used to calculate the control point displacements, and RBF-based deformation technique (control points selection method as shown in Fig. 3) was used to update the 3D structure (Li and Feng, 2007). The optimization objective function values were recorded until the results converged. The entire optimization process consisted of 15 iteration steps and required 10.6 h for completion. Through the above optimization, the axial force, hydraulic efficiency, and head of the impeller were changed from 984.166 N, 93.376%, and 21.756 m to 946.986 N, 96.571%, and 21.752 m, respectively. The iteration curves of the axial force and efficiency are shown in Fig. 5, and the iteration curve of the head is shown in Fig. 6. It can be observed that the axial force is reduced by approximately 3.8%

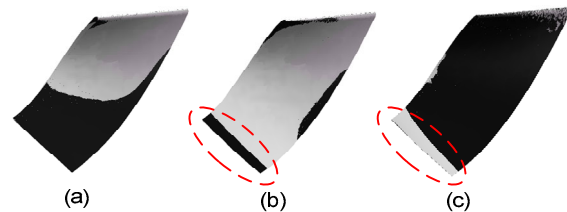


Fig. 4 Blade deformation trends corresponding to different objective functions

(a) Deformation trend of the efficiency function; (b) Deformation trend of the axial force function; (c) Deformation trend of the head function (the dark color indicates that the areas deforming along the normal outward direction increase the objective function, and the opposite is indicated by the light color)

Table 3 Orthogonal test records of factors

Factor of efficiency function	Factor of axial force function=50		Factor of axial force function=60		Factor of axial force function=70	
	Axial force change (%)	Efficiency change (%)	Axial force change (%)	Efficiency change (%)	Axial force change (%)	Efficiency change (%)
50	0.04	0.08	-0.08	0.15	-0.28	0.15
60	0.05	0.11	-0.15	0.17	-0.32	0.18
70	0.07	0.14	-0.11	0.23	-0.30	0.27

after the optimization, the efficiency is increased by approximately 3.2%, and the head is maintained at 21.75 m.

Fig. 7 shows a comparison of the impeller blade shapes before and after the optimization. From the figure, it can be observed that the main deformation

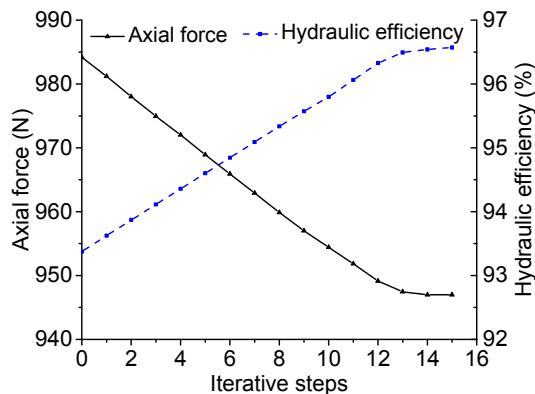


Fig. 5 Iterative curves of the axial force and efficiency

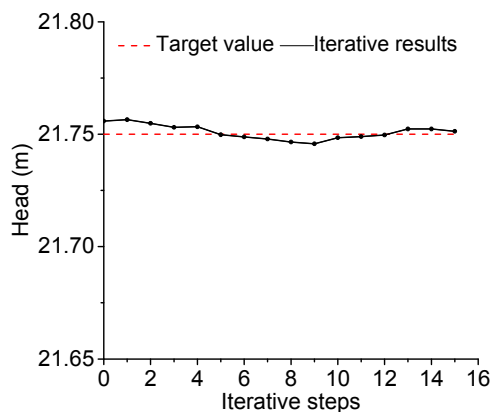


Fig. 6 Iterative curve of the head

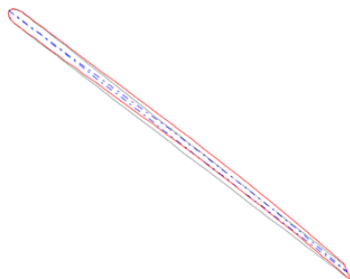


Fig. 7 Comparison of the projection of the impeller before and after optimization

The display image has a 0.5-span cross section, in which the red boundary line is the optimized contour (for interpretation of the references to color in this figure, the reader is referred to the web version of this article)

area of the impeller blade is located in the lower half of the blade near the outlet. The displacement information of the blade was obtained from the optimization result, as shown in Fig. 8. The area with negative values is deformed inward to the fluid domain; the opposite is the case for the area with positive values. The deformation of the pressure surface is consistent with that of the suction surface, so the blade thickness does not change substantially after the deformation. The distribution trend along the channel direction indicates that the deformation directions of the areas near the front shroud and the rear areas are different.

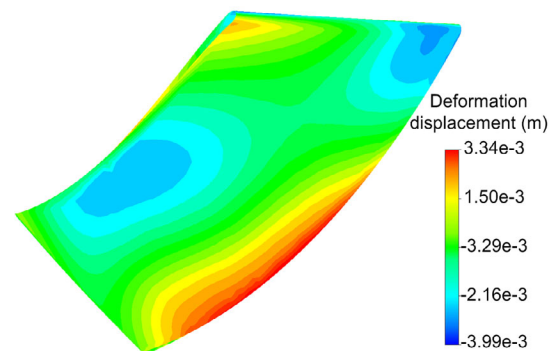


Fig. 8 Deformation displacement map of the blade (suction surface)

4.3 Flow field comparison before and after optimization

The flow fields of the initial and optimized models are now compared. The static pressure distribution comparison is presented in Fig. 9. As the pressure difference between the suction surface and pressure surface of the blade is the main reason for the axial load of the blade (the pressure term in Eq. (9)), the static pressure distributions before and after optimization are different. The static pressure values at the inlet and outlet parts are almost unchanged because of the restricted head, but in the middle of the channel, the main changes occur; the static pressure of the suction surface increases, while the static pressure on the pressure surface increases near the inlet end and remains almost unchanged near the outlet. Fig. 10 shows a comparison of the velocity distributions in the flow passage, in which the velocity variation in the fluid region near the blade is

non-uniform. As the flow separation is an important cause of the decline in efficiency, it is desirable to adjust the blade structure to avoid flow separation to improve the efficiency of the impeller. After the optimization, the low-speed zone near the suction surface and high-speed zone near the pressure surface become thinner. In summary, the shape of the blade is changed to improve the pressure distribution on both sides and reduce the flow loss in the passage under the condition that the outlet edge is almost unchanged. However, because the hydraulic characteristics of the initial model in this study are not very poor, the difference between the pre-optimization and post-optimization is small.

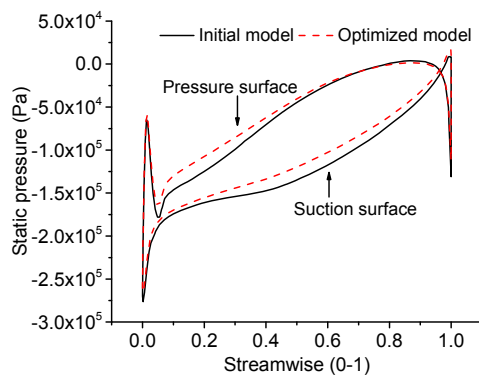


Fig. 9 Comparison of the static pressure distributions on both sides of the blade at 0.5 span

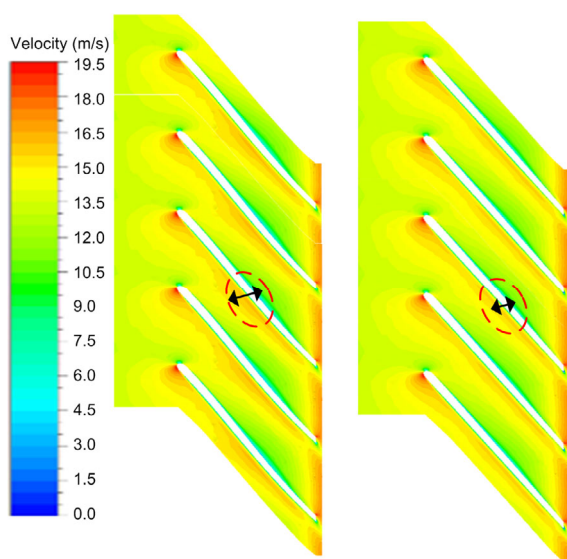


Fig. 10 Contrast maps of the velocity distributions at 0.5 span

4.4 Discussion

The proposed method has many advantages. Compared with the traditional stochastic algorithms, this method does not require large calculations and can update the model with an efficient and accurate optimization path. Furthermore, the method can decouple multiple optimization targets and preferentially optimize regions where the gradient vectors of each target are in the same direction. Moreover, in the RBF deformation, the control points are evenly arranged on the spans of the blade, so that the model boundary is smooth, and the mesh quality meets the fluid calculation requirements.

However, there are still some difficulties with practical applications. For example, if the deformation is too large, some grids may not have a negative volume. We think that the automatic mesh reconstruction can solve this problem, and can be explored in future work. In addition, as a gradient optimization algorithm, the solution obtained with the adjoint method is prone to falling into the local optimum, which indicates that optimization results are usually close to extreme points near the initial parameter point, rather than the maximum point of the entire design space. In future research, we will address this limitation by combining the proposed method with stochastic algorithms.

5 Conclusions

In this study, the adjoint method in a rotating coordinate system based on the RBF is proposed to optimize the impeller of an RCP. Through optimization, the axial force is reduced by approximately 3.8%, and the hydraulic efficiency of the impeller is increased by approximately 3.2%, while the head is kept at a target value. While ensuring the hydraulic performance of the impeller, we achieved load reduction of water-lubricated bearings, which helps to enhance the safety of the RCP. From the optimized result, we find that the lower half of the blade near the outlet edge is the key region in this study. The main significance of this study is as follows:

1. Compared with traditional stochastic algorithms, this method avoids the use of a large number of sample points to find the optimal path and can

directly iterate along the gradient direction to optimize the model.

2. The optimization method combines the adjoint solution with the RBF-based mesh deformation, so the flow calculation and structural deformation are executed automatically, which ensures smooth and efficient updating of the flow field mesh.

3. After optimization, the axial force and hydraulic efficiency of the impeller are improved. The obtained results validate the feasibility of the adjoint method in the optimization design of centrifugal pumps.

4. Based on the results from this study, this method can also be extended to optimize the performance of other hydraulic loads, such as pressure fluctuation.

Contributors

Peng-fei WANG designed the research. Jia-ming WANG and Xu ZHANG processed the corresponding data. Jia-ming WANG wrote the first draft of the manuscript. Xiao-dong RUAN and Xin FU helped to organize the manuscript. Jia-ming WANG and Peng-fei WANG revised and edited the final version. Peng-fei WANG, Xiao-dong RUAN, and Xin FU provided funding acquisitions.

Conflict of interest

Jia-ming WANG, Peng-fei WANG, Xu ZHANG, Xiao-dong RUAN, and Xin FU declare that they have no conflict of interest.

References

- Derakhshan S, Pourmahdavi M, Abdollahnejad E, et al., 2013. Numerical shape optimization of a centrifugal pump impeller using artificial bee colony algorithm. *Computers & Fluids*, 81:145-151.
<https://doi.org/10.1016/j.compfluid.2013.04.018>
- Dong W, Chu WL, 2015. Influence of balance hole diameter on performance and balance chamber pressure of centrifugal pump. *Transactions of the Chinese Society for Agricultural Machinery*, 46(6):73-77 (in Chinese).
<https://doi.org/10.6041/j.issn.1000-1298.2015.06.011>
- Du YY, Liu L, Liu G, et al., 2016. Study of axial force on impeller of mixed-flow pump by unsteady large eddy simulation. *Fluid Machinery*, 44(11):15-19 (in Chinese).
<https://doi.org/10.3969/j.issn.1005-0329.2016.11.004>
- Dwight RP, Brezillon J, 2006. Effect of approximations of the discrete adjoint on gradient-based optimization. *AIAA Journal*, 44(12):3022-3031.
<https://doi.org/10.2514/1.21744>
- ESI-OpenCFD, 2007. OpenFOAM: the Open Source CFD Toolbox. OpenCFD Ltd, Bracknell, UK.
<https://www.openfoam.com/>
- Gao H, Ga F, Zhao XC, et al., 2013. Analysis of reactor coolant pump transient performance in primary coolant system during start-up period. *Annals of Nuclear Energy*, 54(54):202-208.
<https://doi.org/10.1016/j.anucene.2012.11.020>
- Gulich JF, 2014. Centrifugal Pumps, 3rd Edition. Springer, Berlin, Germany, p.495-505.
- Hsin CY, Chen KC, Tzeng YW, et al., 2010. Application of the adjoint method to the propeller designs. *Journal of Hydrodynamics*, 22(S1):484-489.
[https://doi.org/10.1016/S1001-6058\(09\)60243-2](https://doi.org/10.1016/S1001-6058(09)60243-2)
- Jameson A, 1988. Aerodynamic design via control theory. *Journal of Scientific Computing*, 3(3):233-260.
<https://doi.org/10.1007/BF01061285>
- Kong FY, Gao CL, Zhang XF, et al., 2009. Computation and experiment for axial force balance of canned motor pump PBN65-40-250. *Transactions of the Chinese Society of Agricultural Engineering*, 25(5):68-72 (in Chinese).
<https://doi.org/10.3969/j.issn.1002-6819.2009.05.12>
- Li MQ, Wang WG, Li CX, et al., 2016. Study on wear debris in water lubricated thrust bearing of nuclear main pump after rig test. *Lubrication Engineering*, 41(9):113-120 (in Chinese).
<https://doi.org/10.3969/j.issn.0254-0150.2016.09.021>
- Li W, Shi WD, Jiang XP, et al., 2012. New method for axial force balance of canned motor pump. *Transactions of the Chinese Society of Agricultural Engineering*, 28(7):86-90 (in Chinese).
<https://doi.org/10.3969/j.issn.1002-6819.2012.07.015>
- Li YC, Feng ZP, 2007. Aerodynamic design of turbine blades by using adjoint-based method and NS equation. ASME Turbo Expo: Power for Land, Sea, and Air, p.1371-1378.
<https://doi.org/10.1115/GT2007-27734>
- Liu W, Duan R, Chen C, et al., 2015. Inverse design of the thermal environment in an airliner cabin by use of the CFD-based adjoint method. *Energy and Buildings*, 104:147-155.
<https://doi.org/10.1016/j.enbuild.2015.07.011>
- Lotz J, Naumann U, Hannemann-Tamas R, et al., 2015. Higher-order discrete adjoint ODE solver in C++ for dynamic optimization. *Procedia Computer Science*, 51:256-265.
<https://doi.org/10.1016/j.procs.2015.05.237>
- Othmer C, 2008. A continuous adjoint formulation for the computation of topological and surface sensitivities of ducted flows. *International Journal for Numerical Methods in Fluids*, 58(8):861-877.
<https://doi.org/10.1002/flid.1770>
- Othmer C, 2014. Adjoint methods for car aerodynamics. *Journal of Mathematics in Industry*, 4(1):6.
<https://doi.org/10.1186/2190-5983-4-6>
- Othmer C, de Villiers E, Weller HG, 2007. Implementation of a continuous adjoint for topology optimization of ducted flows. Proceedings of the 18th AIAA Computational Fluid Dynamics Conference, p.3947-3954.
<https://doi.org/10.2514/6.2007-3947>

- Papoutsis-Kiachagias EM, Giannakoglou KC, 2016. Continuous adjoint methods for turbulent flows, applied to shape and topology optimization: industrial applications. *Archives of Computational Methods in Engineering*, 23(2): 255-299.
https://doi.org/10.1007/s11831-014-9141-9
- Papoutsis-Kiachagias EM, Kyriacou SA, Giannakoglou KC, 2014. The continuous adjoint method for the design of hydraulic turbomachines. *Computer Methods in Applied Mechanics and Engineering*, 278:621-639.
https://doi.org/10.1016/j.cma.2014.05.018
- Poirier V, Nadarajah S, 2012. Efficient RBF mesh deformation within an adjoint-based aerodynamic optimization framework. Proceedings of the 50th AIAA Aerospace Sciences Meeting Including the New Horizons Forum and Aerospace Exposition, p.59.
https://doi.org/10.2514/6.2012-59
- Rahim FC, Yousefi P, Aliakbari E, 2012. Simulation of the AP1000 reactor containment pressurization during loss of coolant accident. *Progress in Nuclear Energy*, 60:129-134.
https://doi.org/10.1016/j.pnucene.2012.05.009
- Rao ZQ, Yang CJ, 2017. Numerical prediction of effective wake field for a submarine based on a hybrid approach and an RBF interpolation. *Journal of Hydrodynamics*, 29(4):691-701.
https://doi.org/10.1016/S1001-6058(16)60781-3
- Rendall TCS, Allen CB, 2009. Efficient mesh motion using radial basis functions with data reduction algorithms. *Journal of Computational Physics*, 228(17):6231-6249.
https://doi.org/10.1016/j.jcp.2009.05.013
- Robinson TT, Armstrong CG, Chua HS, et al., 2012. Optimizing parameterized CAD geometries using sensitivities based on adjoint functions. *Computer-Aided Design and Applications*, 9(3):253-268.
https://doi.org/10.3722/cadaps.2012.253-268
- Si ZB, Wang G, Guo YY, 2012. Analysis on thrust watts stress field of water lubrication thrust bearing. *Lubrication Engineering*, 37(6):57-59 (in Chinese).
https://doi.org/10.3969/j.issn.0254-0150.2012.06.013
- Su SZ, Wang PF, Xu ZB, et al., 2017. Study on maximum speed setting standard during speed up process of reactor coolant pump. *Nuclear Power Engineering*, 38(5):101-105.
https://doi.org/10.13832/j.jnpe.2017.05.0101
- Tammisola O, Juniper MP, 2015. Adjoint sensitivity analysis of hydrodynamic stability in a gas turbine fuel injector. ASME Turbo Expo: Turbine Technical Conference and Exposition, p.1-10.
https://doi.org/10.1115/GT2015-42736

Zhang JY, Zhu HW, Chun Y, et al., 2011. Multi-objective shape optimization of helico-axial multiphase pump impeller based on NSGA-II and ANN. *Energy Conversion and Management*, 52(1):538-546.

https://doi.org/10.1016/j.enconman.2010.07.029

Zhou FM, 2017. Research on the Hydraulic Design of Canned Nuclear Coolant Pump with High Efficiency, Low Axial Force and Low Hydraulic Pulsation. PhD Thesis, Dalian University of Technology, Dalian, China (in Chinese).

中文概要

题目: 基于伴随求解的核主泵轴向力优化方法

目的: 核主泵轴向力过大容易造成水润滑轴承磨损, 因此在保证扬程和效率性能的同时需要降低核主泵轴向力。本文旨在建立目标性能与叶轮几何形状的函数关系, 探究基于伴随求解的扭曲叶轮的变形方案, 在保证扬程不变的条件下同步优化叶轮的轴向力和效率, 并找到影响该综合性能的叶轮关键区域。

创新点: 1. 提出一种同步改进多个目标性能的叶轮形状优化方法; 2. 将伴随求解和径向基函数网格变形相结合以实现核主泵叶轮三维曲面优化。

方法: 1. 通过理论分析, 建立基于径向基函数网格变形的伴随优化方法, 并在开源平台编写迭代程序; 2. 通过公式推导, 构建扬程、效率和轴向力对应的目标函数 (公式 (19) ~ (21)), 并运用正交实验确定各个目标函数的参数因子; 3. 通过迭代计算, 在保证扬程不变的条件下实现轴向力和效率的同步优化, 确定影响该综合性能的关键区域 (图 8), 并获得叶轮的改进设计方案; 4. 通过流场分析, 对比改进前后流场内部的压力和流速分布情况 (图 9 和 10), 并验证改进方案的可行性和有效性。

结论: 1. 与传统的随机算法相比, 该优化方法直接沿梯度方向进行迭代优化, 可以避免使用大量样本数据来寻找优化路径; 2. 该优化方法将伴随求解和径向基函数网格变形相结合, 实现了流场计算和结构变形的自动化, 可以保证流场网格光滑高效地更迭; 3. 叶轮靠近出口边的下半部分是同步优化核主泵轴向力和效率的关键区域。

关键词: 核主泵; 伴随方法; 径向基函数; 轴向力; 形状优化